Ab Initio Simulations Reveal that Reaction Dynamics Strongly Affect Product Selectivity for the Cracking of Alkanes over H-MFI
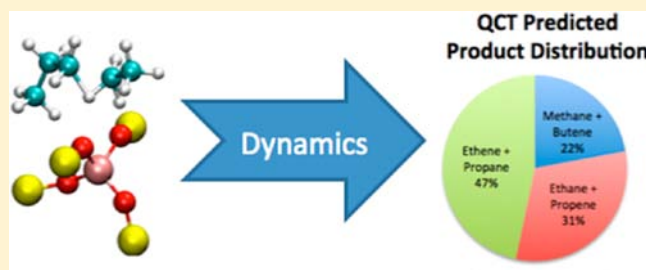
Paul M. Zimmerman, Diana C. Tranca, Joseph Gomes, Daniel S. Lambrecht, Martin Head-Gordon,* and Alexis T. Bell*

Department of Chemical and Biomolecular Engineering, University of California Berkeley, California 94720-1462, United States
Department of Chemistry, University of California Berkeley, California 94720-1461, United States

Ⓢ *Supporting Information*

ABSTRACT: Product selectivity of alkane cracking catalysis in the H-MFI zeolite is investigated using both static and dynamic first-principles quantum mechanics/molecular mechanics simulations. These simulations account for the electrostatic- and shape-selective interactions in the zeolite and provide enthalpic barriers that are closely comparable to experiment. Cracking transition states for *n*-pentane lead to a metastable intermediate (a local minimum with relatively small barriers to escape to deeper minima) where the proton is shared between two hydrocarbon fragments. The zeolite strongly stabilizes these carbocations compared to the gas phase, and the conversion of this intermediate to more stable species determines the product selectivity. Static reaction pathways on the potential energy surface starting from the metastable intermediate include a variety of possible conversions into more stable products. One-picosecond quasiclassical trajectory simulations performed at 773 K indicate that dynamic paths are substantially more diverse than the potential energy paths. Vibrational motion that is dynamically sampled after the cracking transition state causes spilling of the metastable intermediate into a variety of different products. A nearly 10-fold change in the branching ratio between C2/C3 cracking channels is found upon inclusion of post-transition-state dynamics, relative to static electronic structure calculations. Agreement with experiment is improved by the same factor. Because dynamical effects occur soon after passing through the rate-limiting transition state, it is the dynamics, and not only the potential energy barriers, that determine the catalytic selectivity. This study suggests that selectivity in zeolite catalysis is determined by high temperature pathways that differ significantly from 0 K potential surfaces.

■ INTRODUCTION

Zeolites are used extensively for the cracking of alkanes, an important step in the processing of petroleum. The products of this reaction are lower molecular weight alkanes and alkenes. For example, the cracking of propane can produce methane and ethene, but as the molecular weight of the alkane increases, the number of stoichiometrically distinct products formed increases dramatically.[1] Because of the importance of alkane cracking, there has been considerable interest from both experimental and computational perspectives in understanding the effects of zeolite structure and Si/Al ratio on the mechanism and kinetics of alkane cracking. Experimental studies have shown that, at low alkane partial pressures and conversions, the reaction proceeds via a monomolecular mechanism.[2,3] An alkane molecule adsorbed in the zeolite is first protonated and then undergoes C−C bond cleavage, which leads ultimately to the formation of lower molecular weight alkane and alkene fragments. However, such studies have not provided clear predictions of how zeolite structure and pore shape dictate the intrinsic distribution of reaction products.[4−21]

Computational analyses of alkane cracking[22−30] have focused on identifying the transition states (TSs) for various types of C−C bond cleavage and determining the associated activation

energies. The implicit assumption in these studies is that each TS leads to a unique reactant/product pair, i.e., those that were specified in carrying out the search for the TS.[31−35] What this approach neglects is the possibility that multiple products might form from a given transition state, that identical products might form from multiple transition states, or that metastable intermediates may exist between the reactants and products. Moreover, the TSs that are located occur on the 0 K potential energy surface and neglect the possibility that the reaction paths at finite temperature may be substantially different. As a result, standard analysis of transition states does not in general provide an adequate basis for predicting product distributions. However, more sophisticated techniques have been reported for case of propane cracking on H−CHA,[36] which was explored through the use of transition-path sampling.[37,38] This study has shown that multiple TSs can lead to similar products and that multiple reaction pathways from a given TS are possible due to the relatively flat potential energy surface (PES) in the zeolite. Motivated by this report, we have investigated the applicability of quasiclassical trajectory simulations (QCT) to provide

information on the distribution of products that can be formed during the cracking of *n*-pentane on H-MFI.

Quasi-classical trajectories provide a chemically meaningful way of investigating complex reaction pathways by use of molecular dynamics simulations. QCTs use the information about the vibrational spectrum of the system to populate the initial velocities of all atoms at a chosen temperature and propagate the nuclear motion classically.[39,40] QCT simulations that begin from a TS identify the pathways via which products are formed at a working reaction temperature and can thus give the distribution of products formed from the chosen TS. The advantages of QCT over purely classical simulation techniques stem from the fact that QCT initial velocities of all atoms are based on quantum mechanical vibrational populations, including zero point energy (ZPE). This is particularly important for systems where ZPEs are large or where C−H bonds are vital to the reactivity. QCT has been used successfully to calculate spectral features,[41] radial distribution functions,[42] and average structures.[43] Most importantly, QCTs have had significant success in determining reaction branching ratios for complex reactions.[44−48]

In this study, we have utilized QCT to sample the dynamic degrees of freedom involved in cracking of *n*-pentane over the zeolite H-MFI. To capture the local chemistry of bond-breaking and forming at the Brønsted-acid site,[49] it is critical to describe not only the local interaction of the adsorbate with the site but also its medium- to long-range nonbonded interactions with the zeolite lattice.[50,51] Full quantum mechanical simulation of the effects of both the local environment of the Brønsted-acid site and the surrounding zeolite can be carried out in principle by methods such as dispersion-corrected density functional theory (DFT). In practice, however, the need to use large zeolite lattices in order to satisfactorily capture the long-range effects of dispersive and Coulombic forces makes such calculations prohibitively expensive.[52−58]

We address this feasibility challenge using a hybrid quantum mechanics/molecular mechanics (QM/MM) approach, in which the local chemistry described with (expensive) QM and the long-range interactions are described (inexpensively) by MM.[56] It is important that these two regions interact in a chemically meaningful way. In our QM/MM approach, the QM region is polarized by the MM region (i.e., electrostatic embedding) using point charges derived from QM to accurately represent the lattice electrostatic potential. A Lennard-Jones potential between the MM region and the substrates describes shape-selective van der Waals interactions with the zeolite framework. This level of theory minimizes computational effort while approaching the accuracy of a hybrid and dispersion corrected density functional.[56]

Our studies described herein reveal that the pathway from the TSs for the rate-limiting steps involved in the cracking of *n*-pentane to the final products proceeds through one or more metastable states on the PES (by metastable, we mean a structure that is a local minimum but has relatively low barriers to escape to lower energy local minima) and that multiple products can form from individual TSs. We also demonstrate that the distribution of products determined from QCT at 773 K is quite different from that estimated on the basis of an analysis of the 0 K PES alone. The qualitative difference between static and dynamic pathways suggests that non-equilibrium reaction dynamics and free energies are key factors determining the distribution of products formed during alkane cracking on zeolites.

■ COMPUTATIONAL METHODS

QM/MM Simulation. H-MFI is represented by a cluster containing 276 tetrahedral atoms (T276), which is illustrated in Figure 1. The atomic positions of the tetrahedral atoms (Si and Al)
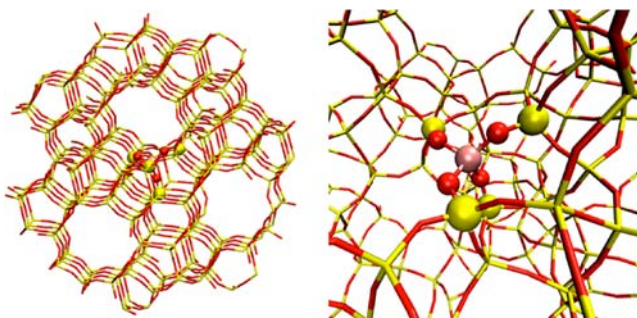

Figure 1. Model MFI cluster with 276 tetrahedral centers. The center Al site, which is the QM region of the QM/MM, is shown with spheres. This cluster captures the shape selective and electrostatic effects of an extended MFI zeolite.

and the bridging O atoms in this cluster were taken from the crystallographic structure of MFI determined from X-ray diffraction.[59] While the distribution of Al in MFI is unknown and depends on the conditions of zeolite synthesis, there is some evidence that the T12 position is favored.[60,61] For this reason, the T12 site was chosen as the location of the Al atom associated with the acid site. The Brønsted-acid site was modeled using a QM region of 5 tetrahedral atoms (T5), shown in Figure 1, and the balance of the cluster was modeled by MM. Hydrogen link atoms were placed along the Si−O bond at R = 92% of the Si−O bond distance and scaled neighboring charges were used to smoothly terminate the QM region. The charges on the atoms located at the cluster surface were scaled such that the cluster had zero net charge.[56] The lattice atoms away from the active region were frozen at their crystallographic positions.

Dynamics simulations were carried out using the B97-D density functional[62] and the 6-31G* basis set. For the portion of the zeolite represented by MM, the charges and Lennard-Jones parameters for Si and O chosen were taken from our previous work in which these parameters had been selected to achieve close agreement with all-QM and experimental values of heats of molecular adsorption and activation energies.[56] The MM charge parameters were 0.7 e and −0.35 e for Si and O framework atoms, respectively. The Lennard-Jones parameters were ε_{Si} = 0.2 kcal/mol, ε_O = 0.075 kcal/mol, R_{Si} = 2.2 Å, and R_O = 1.77 Å for the framework atoms. Lennard-Jones parameters for hydrocarbons were taken from CHARMM.[63] Although optimized geometries from the B97-D/6-31G* level of theory were used to minimize computational effort in the dynamics simulations, additional optimizations were performed using dispersion-corrected range-separated ωB97X-D functional[64] and the triple-ζ 6-311G** basis to obtain high-quality thermodynamics for the rate-limiting barriers. Transition states were found using a combination of the Freezing String Method[34] and eigenvector following approaches.

Frequency computations were performed on all intermediates to ensure that geometries corresponded to local minima (zero negative eigenvalues) or transition states (one negative eigenvalue). Intrinsic reaction coordinate (IRC) computations[65] were performed to locate the steepest descent, nondynamic path on the 0 K surface from each TS. TS energies were zero-point corrected and further converted to enthalpies and free energies at 773 K using the harmonic oscillator approximation. All simulations were performed utilizing a development version of the Q-Chem software package.[66]

Reaction Path Simulations. Direct dynamics simulations, in which the energy and force are computed via ab initio theory at each time step, were carried out in order to investigate the pathways followed from the TS for the cleavage of each C−C bond. In contrast to most molecular dynamics simulations that populate free particle

velocities from a Boltzmann distribution, QCT trajectories were initiated with velocities that are consistent with QM populations of each harmonic vibrational mode based on the canonical ensemble (773 K) at the TS structure. The QCT approach assures that the initial nuclear velocities are selected so as to represent the quantum effects of nuclear motion and, most importantly, that each mode contains at least ZPE. The energy from these vibrations was placed into the kinetic energy of each normal mode, and these vibrations were converted to Cartesian velocities to start the trajectory. To this end, we modified the QCT implementation of Lambrecht et al.[41] so that the transition state mode was populated in a specified direction (i.e., forward or reverse) along with the remaining vibrational modes. A more complete sampling approach would be to initiate trajectories with randomized displacements (e.g., at constant total energy) along the vibrational modes.[67,68] Each microcanonical trajectory was integrated for a total of 1 ps with a time step of 0.5 fs.

Three types of reaction path simulations are compared: MEP from IRC steepest descent simulations, a dynamic reaction coordinate (DRC),[40] and QCT. The MEP is essentially a zero velocity trajectory, with no corner cutting. The DRC simulation is a single trajectory[69] that is initiated by nudging the system forward along the TS mode, while all orthogonal modes are initiated at zero velocity. Thereafter energy is conserved, and therefore the DRC provides a minimum description of system dynamics starting at the TS while excluding the influence of (initial) nuclear motion in the vibrational modes orthogonal to the TS. DRC is thus a model that lies between IRC and QCT in which some, but not all, effects of dynamics are taken into account.

■ RESULTS AND DISCUSSION

Static Description of *n*-Pentane Cracking in H-MFI. Key geometries for the interaction of *n*-pentane with the Brønsted acid site of the H-MFI clusters were located using QM/MM and are shown in Figure 2. While there are many
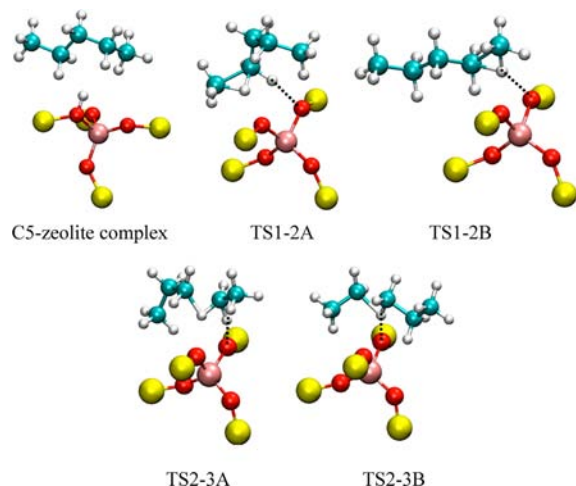
Figure 2. The *n*-pentane reactant complex and three unique C5 cracking transition states. The dotted line represents the path from the oxygen to the attacking proton. Only the zeolite atoms belonging to the acid site are shown for clarity (see Figure 1 for the full cluster model).

possible conformations for absorption of *n*-pentane at the acid center associated with the T12 Al site, these conformations are isoenergetic to within about 1.0 kcal/mol and therefore can plausibly be represented by a single conformation. The use of a single conformation means there not all relevant TSs will be located because additional TSs exist starting from other conformations. However, as will be clear below, this conformation should still provide a good reference point for

computing intrinsic reaction barriers because they are associated with local bond-breaking that is largely independent of conformation.

Because *n*-pentane has two distinct C−C bonds, cleavage can occur at either one.[70] The TSs associated with cracking at the 1−2 and 2−3 C−C bonds are denoted as TS1−2 and TS2−3. These transition states are further divided into pairs of unique saddle points, denoted by the letters A and B (TS1−2A and TS1−2B; TS2−3A and TS2−3B) that differ by the manner in which protonation occurs. In configuration B, the proton approaches the C−C bond directly and cleaves it. In configuration A, the proton approaches the second carbon (labeled starting from the terminal carbon in the chain), causing H transfer to occur along the carbon chain as shown in Scheme 1. It is this second hydrogen that splits the C−C bond.

Scheme 1. Cracking TSs Investigated in This Study
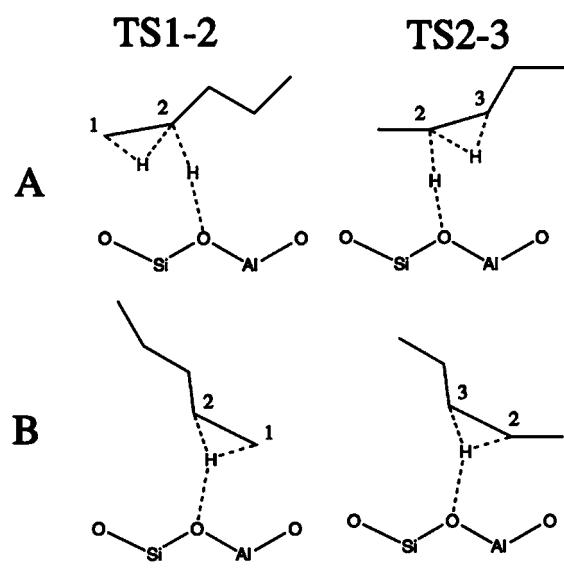
Another reaction, not shown, can occur if the *terminal* carbon of *n*-pentane is protonated and the neighboring C−C bond is then cleaved. Since the energy of this TS is 6 kcal/mol higher than that for TS1−2A, we have not considered this pathway further.

The intrinsic activation enthalpies of the four transition states considered in this study are presented in Table 1. Differences between the experimental and calculated activation enthalpies are not unexpected, as the experimental value results from cracking occurring at a distribution of acid sites in H-MFI, whereas the simulation results are for a specific acid site (and conformation). Nevertheless, the activation enthalpies calculated at 773 K are close to the value reported experimentally for *n*-pentane cracking.[71−73]

IRC analysis was performed to obtain the minimum energy path connecting each transition state to the nearest reactant and product states. On the reactant side, the IRCs all lead to the expected reactant state, i.e., *n*-pentane adsorbed at the acid site, as shown in Figure 3. On the product side of each of the transition states, the IRC paths end at a high-energy, metastable local minimum characterized by a proton shared between two fragments (denoted as C−H−C intermediate). The structures of the C−H−C intermediates are shown in Figure 4 for TS2−3 and are seen to be quite different from the stable product states that may have been expected to form from this TS. A Mulliken

Table 1. Intrinsic Activation Energies in kcal/mol for Cracking of *n*-Pentane at the T12 Al Position in the 276 Tetrahedral Atom MFI Model Using wB97X-D/6-311G*[a]**

	E_a (0 K)	$\Delta H^{\dagger}$ (773 K)	$\Delta G^{\dagger}$ (773 K)	experiment $\Delta H^{\dagger}$ (773 K)
TS1−2a	44.1	44.6	47.0	42.5 ± 2.0^{a}
TS1−2b	41.8	42.6	44.6	(Si/Al experiment: 35)
TS2−3a	40.0	40.5	42.2	
TS2−3b	47.8	48.4	49.9	

[a]Intrinsic activation energies obtained from apparent activation energies of refs 71 and 72 added to absorption energies from ref 73.

Figure 4. Optimized metastable intermediates from immediately after cracking TS2−3A (left) and TS2−3B (left) as predicted by DRC and IRC. While most of these intermediates quickly fragment in QCT into more stable intermediates, a small fraction remain after 1 ps.
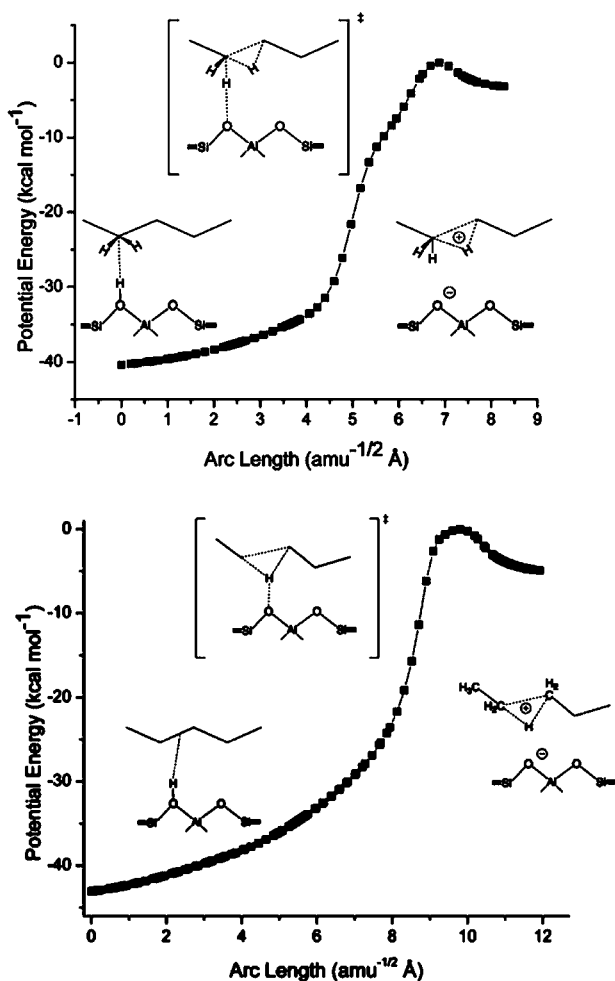
Figure 3. IRC pathways for cracking TS2−3A (top) and TS2−3B (bottom). All IRC paths arrive in the reverse direction with pentane coordinated to the acid site, while the forward direction IRC paths end at C−H−C quasistable intermediates.

charge analysis of these intermediates is shown in Figure 5 and compared with those for the analogous free carbocation in the gas phase. The strong resemblance of the structures and charge distribution for the intermediates of cracking and of free carbocations indicates that the intermediates are carbocations stabilized by the electrostatic interactions with the zeolite framework. Further analysis reveals that the extended zeolite lattice electrostatically stabilizes the carbocations by about 15 kcal/mol (by comparison of energy of the intermediate to the reactant complex with or without electrostatic stabilization from the extended lattice), so the existence of stable carbocation intermediate states is a direct consequence of the electrostatic environment.
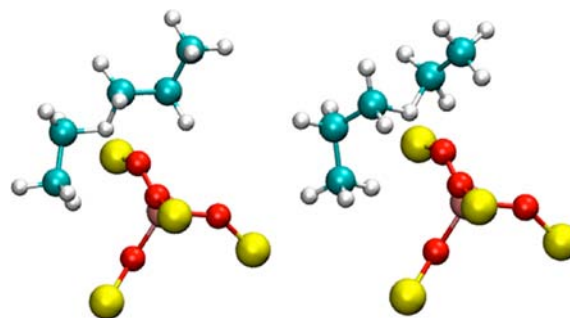
A rich maze of reaction pathways leading from the metastable intermediate to ethene−propane and propene−ethane were identified by analysis of the PES and are shown in Figure 6. All of the energies shown in this figure are referenced to that of the metastable intermediate formed by passage of the system through TS2−3A. Similar diagrams could be drawn for the other TSs but only the features on the PES for TS2−3A were chosen for further analysis because TS2−3A is the TS with the lowest energy barrier. Figure 6 shows four unique TSs: one that leads to propane and ethoxide, one that leads to ethane and propoxide, one that leads to ethene and propane, and one that leads to propene and ethane. The two TSs to alkoxides have barriers lower than that for TS2−3A and represent S_N2-like reactions between the carbon fragment and the resulting alkane. These transformations are particularly facile because the energy cost for nuclear rearrangement required to displace the C−H−C linkage with an alkoxide bond is low. However, the remaining two TSs have higher barriers that lie above that for TS2−3A. Examination of Figure 6 suggests that the metastable intermediate will decompose via two low-barrier paths to form C2 and C3 alkoxide intermediates and the corresponding C3 and C2 alkanes. The C2 and C3 alkoxides can then react with moderate barriers to form the corresponding C2 and C3 alkenes.

The reaction pathways shown in Figure 6 suggest that reactants passing through TS2−3A will form a metastable C−H−C intermediate, which will react to form C2 and C3 alkanes, alkoxides, and alkenes. The product distribution resulting from these reaction pathways can be estimated assuming that all species are in thermal equilibrium and that the steady-state assumption is applicable (see Supporting Information). The results of this analysis suggest that the ratio of propene−ethane to ethene−propane should be 0.07, which is much lower than the experimentally observed value of 2.9.[71,72] As discussed below, this significant discrepancy is due in large part to the assumption that all species are thermally equilibrated and to the
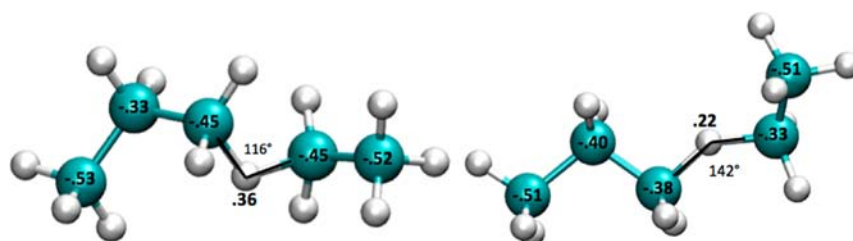
Figure 5. Charge analysis (Mulliken) of the C−H−C intermediate in the zeolite (left) compared to the gas-phase carbocation (right). The gas-phase carbocation is relaxed from the zeolite structure to its local minimum. In the vacuum the C−H−C angle widens to stabilize the proton between the two hydrocarbon fragments, but otherwise the molecular geometries are similar between the two cases.
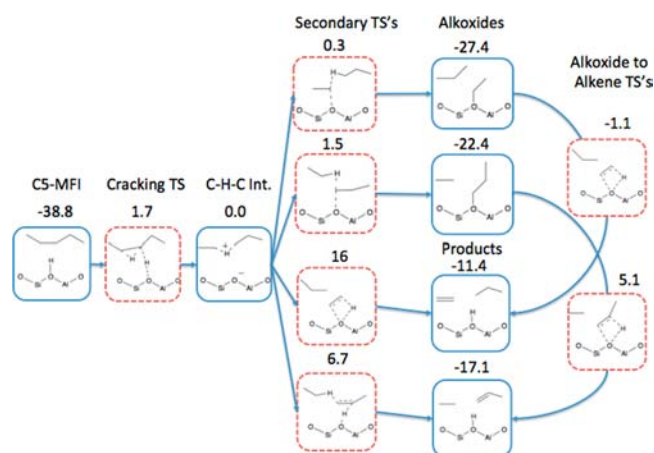

Figure 6. Key intermediates and transition states on the PES for TS2−3A (energies in kcal/mol). Dynamical considerations can lead to significantly different distributions of alkanes and alkenes than would be inferred from this information alone.

neglect of the effects of nonequilibrium dynamics and entropy on the course of the reaction.

Dynamic Description of *n*-Pentane Cracking. Molecular dynamics simulations of the system as it evolves from the transition state toward the products were performed using DRC and QCT. Trajectories were initiated at the TS and run for 1 ps, a time that is typically sufficient for the system to fragment into relatively stable species. A plot of critical C−H and C−C bond distances taken from the DRC simulation starting at TS2−3B is given in Figure 7. The DRC is the trajectory for which the vibrational modes orthogonal to the TS
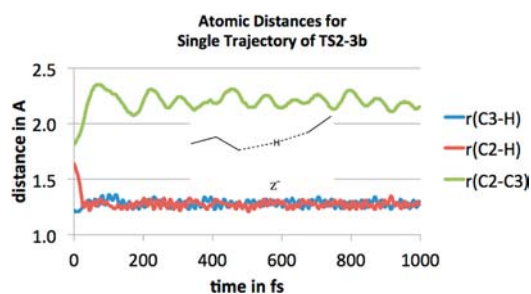

Figure 7. Atomic distances during the DRC for TS2−3B. $r(C3−H)$ refers to the distance between the reactive H and the terminal carbon on the C3 end, $r(C2−H)$ similarly for the C2 carbon. $r(C2−C3)$ is the distance between the two carbons where the bond breaking occurs. DRC settles into a quasistable region where the proton is shared between the two carbocationic fragments, and the final product from the TS is not yet determined.

are initially inactive, but the potential energy is converted into kinetic energy along the direction of the TS eigenvector. Within about 50 fs, the system settles into the quasistable C−H−C intermediate, and at later times, vibrations of the C−H−C bond formed by insertion of the proton into the C−C between the C2 and C3 fragments can be observed. The intermediate discovered by DRC oscillates around the minimum identified by following the IRC in the product direction starting from TS2−3A. However, the DRC trajectory does not result in the formation of any final products. This observation leads to the inference that vibrational motion orthogonal to the TS mode is important in determining the reaction products.

By contrast, QCT simulations reveal the full spectrum of products that form from a TS. A series of frames taken from a few of the trajectories are shown in Figure 8. See the
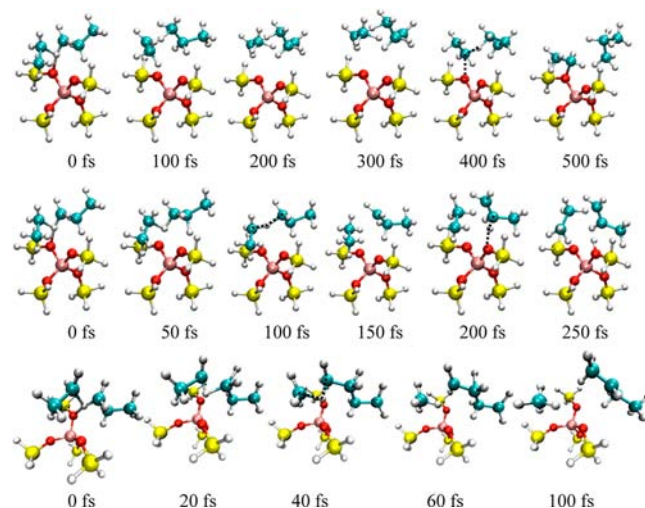
Figure 8. Snapshots of trajectories from TS2−3B. Top: ethoxide formation. Middle: propene formation. Bottom: methane formation. Ethoxide and propene formation are common, but only one trajectory led to methane formation.

Supporting Information for videos of additional trajectories. In the first trajectory (I), the acidic hydrogen is shared by the C2−C3 fragments for the first 400 fs. After about 400 fs, the hydrogen is transferred to the C3 fragment, forming propane. This leaves the C2 fragment as $C_2H_5^+$, which can either deprotonate or form an ethoxide species bound to the zeolite surface. By 500 fs, the C2 fragment becomes an ethoxide that is stable for the remainder of the trajectory. The second trajectory (II) experiences a similar sharing of the acidic H for more than the first 100 fs. By 150 fs, however, the hydrogen has transferred to the C2 fragment to form ethane. The C3 carbocation subsequently deprotonates by proton transfer to

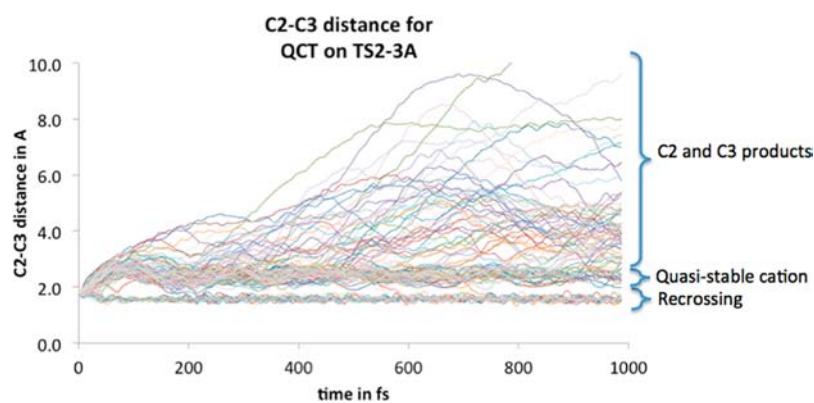**Figure 9.** C2−C3 distance as a function of time for the QCT simulations of TS2−3A. The trajectories are grouped into those that recross to the reactant state, the quasistable carbocations formed immediately after the TS, and the C2/C3 products after completely severing the C−C bond.

the active site, yielding propene by 250 fs. The third trajectory (III) is more surprising. Within 30 fs, the attacking proton shifts down the C5 chain to attack the C1−C2 carbon bond instead of the C2−C3 bond. After 60 fs, methane and an *n*-butyl carbocation are formed, and at later times (not shown), the *n*-butyl carbocation deprotonates to produce 1-butene. These three examples demonstrate that the system can evolve from a single rate-limiting transition state into the metastable C−H−C intermediate and then rapidly proceed further downhill to a variety of stable products. The time scale of these transformations is less than 1 ps, which suggests that the metastable intermediate does not have sufficient time to thermally equilibrate. The product distribution therefore can be found by sampling many trajectories proceeding from the TS.

To sample the evolution of the C−H−C intermediate into more stable products, 100 trajectory simulations were performed starting from TS2−3A and TS2−3B. Figure 9 illustrates how the trajectories initiated from TS2−3A arrive at the resultant products. In particular, the distance between the two carbons that are cleaved are shown as a function of time. In the first 50 fs, most of the trajectories follow a similar path from the TS to the C−H−C intermediate, apart from some barrier recrossing trajectories that deprotonate within the first 20 fs, leading toward the reactant complex. Periods along the reacting trajectories can be seen in which the C−C distances are of intermediate length (1.9−2.3 Å), indicating the C−H−C carbocation. At later times, most trajectories lead to cleavage of the C−C bond as illustrated by the growth in the C−C bond distance. This separation is constrained by the zeolite framework, so products can diffuse away from the active site by only a few angstroms within the 1 ps trajectory. It can also be seen that a number of trajectories recross to the reactant complex at later times, as evidenced by a decrease in the C2−C3 bond distance. The wide spread of C2−C3 distances across the various trajectories strongly suggests that dynamic pathways sample a much wider range of reaction channels than those predicted by IRC and DRC simulations.

The distribution of intermediates determined from an analysis of these 100 trajectories is shown in Table 2. Fewer trajectories (∼15) were performed starting from the TS1−2A and TS1−2B transition states because only methane and butene were observed as stable products. The major products deriving from TS2−3A and TS2−3B after 1 ps of simulation were ethoxide and propane, ethene and propane, propoxide and ethane, propene and ethane, and C−H−C carbocations. Infrequently observed products from TS2−3 are H_2 and

Table 2. Intermediate Distributions from QCT for C5 Cracking TS2-3A and TS2-3B for a Total of 100 1-ps Trajectories on Each TS[a]

	reaction	
	TS2−3A	TS2−3B
recrossing	19%	19%
C−H−C carbocation	19%	7%
C_2^+ + propane	23%	6%
ethene + propane	12%	2%
C_3^+ + ethane	21%	38%
propene + ethane	2%	22%
methane + butene	0%	1%
cyclopropane + ethane	3%	5%
H_2 + pentene	1%	0%

[a]These intermediates convert to the final products listed in Table 3 at time scales longer than the QCT simulations.

pentene, methane and butene, and cyclopropane (less than 5% total). About 19% of the trajectories recrossed to yield the reactant complex from which it can be concluded that overall transmission coefficient is 0.81.

The intermediate distributions from the trajectories are shown in Table 2 and Figure 10. The two most abundant intermediates derived from an analysis of QCT started at TS2−3A and TS2−3B are C2 and C3 alkoxides. However, the distribution of intermediates (Table 2) also shows substantial fractions for products that are predicted to have low probability of formation based on an analysis of the PES (see Figure 6 and the previous part of Results and Discussion). At 773 K, the potential energy barriers suggest that the relative yield of ethene (through the lowest energy path) would be low because the barrier for ethene formation is ∼10 kT, whereas other channels have barriers less than kT. However, this conclusion does not take into consideration the effect of dynamics. For example, QCTs initialized from TS2−3A show significant formation of ethene after 1 ps (Table 2) suggesting that dynamical effects make direct ethene formation from the C−H−C intermediate significantly more viable than inferred from the potential energy barrier. Similarly, the PES predicts that for each ethoxide formed, 0.4 trajectories will recross back to the reactant state. In QCT, however, 0.8 trajectories recrossed per ethoxide formed.

Some of the QCT initialized from TS2−3 produced H_2 and pentene, methane and butene, and cyclopropane; these are products that would not have been expected based on the analysis of the PES. Starting from a relatively high-energy TS,
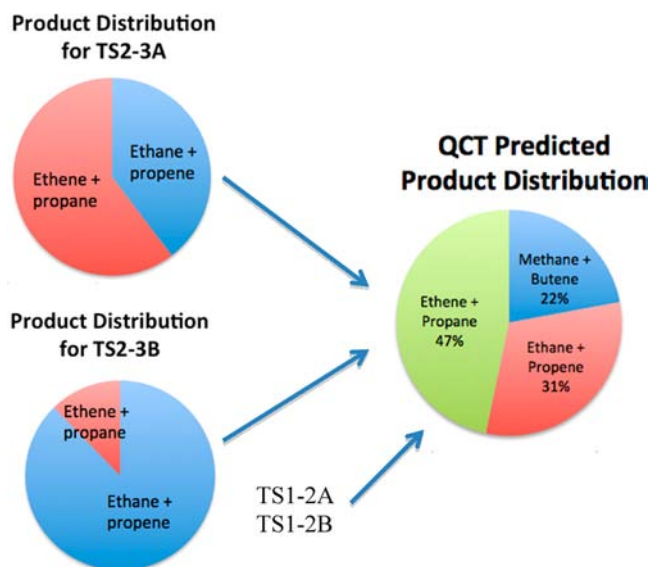
Figure 10. Final product distributions from trajectories, which are combined using harmonic oscillator estimates of the free energy barriers to obtain the overall product distribution at 773 K. Minor products are not shown (such as pentene).

vibrational excitation in modes perpendicular to the TS can result in migration of the system toward areas of the reactive landscape that would not be sampled by MEP or DRC simulations.

The differences in the intermediate distributions determined from the PES vs those predicted with QCT dynamics can be understood via two possible explanations. One is that the free energy barriers for the TSs leading out of the metastable intermediate differ from the potential energy barriers. While selectivity to some products may agree well with the PES prediction, other selectivities are in error by factors of two or more. This implies that at reaction temperatures, the entropic contribution to the barrier height may be large. For this reason, it would be desirable to compute free energy barriers. Unfortunately, the standard harmonic oscillator approximation (used, e.g., in Table 1) is known to perform relatively poorly for determining free energies when there are many soft degrees of freedom. On the other hand, while thermodynamic integration is conceptually possible, it is quite costly for ab initio simulations, because trajectories orders of magnitude longer than 1 ps are required.[74]

A second explanation may be that for short periods after passing through a rate-limiting TS, nonequilibrium dynamics affect the reactivity. This effect is included in QCT, which follows high-T microcanonical pathways that are substantially different than the PES paths. Instead of relying on the assumption of equilibrium at all times, QCT simulations populate vibrational modes at the reaction temperature (with equilibrium sampling at the TS only). This allows QCT trajectories to follow reaction paths that are related qualitatively to the accessible free energy paths after the TS, where the free energy paths represent thermodynamic averages at high temperature over the many possible reactive trajectories. This sampling procedure allows QCT to determine high-temperature intermediate distributions while only requiring the assumption that the system does not equilibrate after the TS on sub-picosecond time scales. The fact that the post-TS

dynamics leading to products is rapid (typically sub-picosecond) suggests that full equilibration may not be achieved.

QCT sampling suggests that the reaction paths leading out of the C−H−C intermediate may be closer together in free energy than would be suggested by the potential barriers shown in Figure 6. This can be qualitatively understood by considering the entropic gains from fragmenting the metastable intermediate into multiple species. The metastable intermediate, being a carbocation, begins by being bound to the Al site by electrostatic interactions (i.e., one molecule at a surface site). Converting this intermediate into an alkane and an alkoxide represents the formation of one "free" molecule in the zeolite. Converting the intermediate into an alkane plus an alkene results in the formation of two free molecules. Although these molecules are confined within the zeolite, they are still higher in entropy than a single molecule that is strongly bound by electrostatics to a single surface site. The TSs leading to these higher entropy intermediates are along the path to the higher entropy states and are therefore likely to have correspondingly higher entropy than the C−H−C intermediate.

The contribution of entropy to the free energy of cracking is illustrated qualitatively in Figure 11. Shown here is the pathway
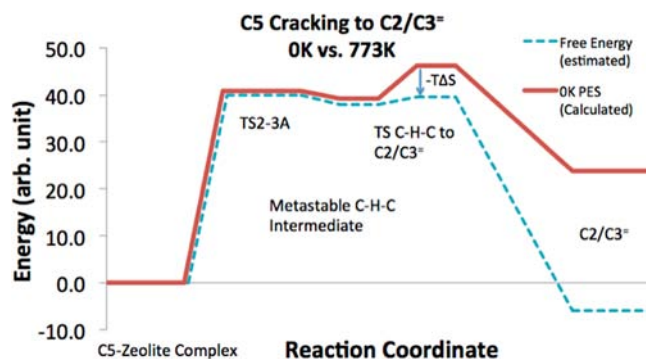

Figure 11. Zero Kelvin PES compared to qualitative free energy surface at 773 K for *n*-pentane cracking leading directly to ethane and propene. The $T\Delta S$ correction applied has the correct sign, but the actual value is arbitrary (see text). Similar PESs could be constructed for the other pathways in Figure 6.

along the PES at 0 K and the pathway envisioned to occur on the free energy surface at 773 K. On the basis of the arguments given above, the entropy of key TSs increases as the reactants proceed toward the products. This lowers the free energy barriers relative to the potential energy barriers on the PES, especially when a new molecule is formed, resulting in a free energy pathway that generally descends from the rate-limiting cracking TS to the alkane and alkene products. The total entropic gain from *n*-pentane to ethene and propane is 41 cal/(mol K) in the gas phase. Adding the reaction enthalpy to this entropic contribution at 773 K translates into a free energy process that is 6.2 kcal/mol downhill. Although as discussed above, we cannot obtain accurate estimates of free energies for each step, qualitative corrections to the potential energy barriers can still be made knowing that entropy increases along the reaction pathway. This procedure applied to the pathway in Figure 11 suggests that the cracking TSs are rate limiting in terms of free energy and that subsequent steps occur rapidly. This agrees well with the predictions from QCT that show the lifetime of the C−H−C intermediate is less than 1 ps.

Final product distributions, determined from QCTs initiated from TS1−2 and TS2−3, can be obtained by Boltzmann weighting of the harmonic oscillator free energy barriers combined with the QCT product distributions for each TS. The harmonic oscillator approximation is not ideal but is used because it is computationally affordable. It is noted that ethoxide and propoxide intermediates can be deprotonated at relatively low barriers to yield ethene and propene, respectively, so the final product selectivity can be estimated from the QCT simulations. The QCT trajectories cannot be considered to be a statistically converged distribution of all C5 cracking reactions, in part due to the single active site chosen for the model and the relatively limited QCT sampling (100 trajectories), but the results are nonetheless illuminating. The final product distribution analysis given in Table 3 and Figure 10 shows

Table 3. Final Product Distributions for Cracking TSs TS1−2 and TS2−3 and Free Energy Weighted (at 773 K) total distribution for T12 Al Position Cracking in H-MFI[a]

	methane + butene	ethane + propene	ethene + propane
TS1−2A	100%	0%	0%
TS1−2B	100%	0%	0%
TS2−3A	0%	40%	60%
TS2−3B	2%	86%	12%
overall	22%	31%	47%
		simulated	experiment[71,72]
$R_{C3=}/R_{C2=}$ (TS2−3A PES)		0.07	2.9
$R_{C3=}/R_{C2=}$ (QCT)		0.7	2.9
R_{C2+C3}/R_{C1+C4} (QCT)		2.0	3.0

[a]The standard errors on these distributions is ±5%.

that C2 and C3 products are dominant, which agrees with the experimental results.[71,72] The ratio of propene to ethene (0.7) is substantially better than that predicted from an analysis of the PES, where this ratio was estimated to be 0.07. However, the ratio is still significantly lower than that found experimentally (2.9). There are several possible reasons for this disagreement: (1) The free energy barrier difference between TS2−3A and TS2−3B may be too high due to the harmonic oscillator approximation or errors in the utilized density functional (a lower barrier on TS2−3B would account for more propene formation); (2) the T12 acid site may have a different product distribution than the ensemble average of Al sites in the experimental catalyst; or (3) other initial conformations of adsorbed pentane at the T12 site may lead to shifts in the relative barrier heights associated with TS2−3A and TS2−3B.

CONCLUSIONS

Reaction dynamics play a vital role in the cracking of *n*-pentane in acidic MFI zeolites. The results presented show that a static PES can provide only an incomplete description of the rate-limiting TSs for catalytic cracking, which is insufficient to accurately determine the selectivity of the reaction. Instead of the barrier for the apparent rate limiting TS alone accounting for selectivity (as in the static PES picture), the short-time dynamics of the C−H−C carbocation formed immediately after the TS heavily influences the products of each cracking TS. This procedure in effect samples the nonequilibrium reaction pathways after the TS, which are substantially different from the potential energy paths. This suggests that the description of potential energy pathways in this system is not sufficient to quantify the product selectivity. To capture product selectivity,

some knowledge of the high-temperature reactivity must be obtained. In this study, the QCT provides such sampling and suggests the potential energy surface may differ greatly from the free energy surface.

Because carbocationic species such as those formed by the protonation of alkane C−C bonds are common and important reactive intermediates in zeolites, their behavior is integral to catalytic processes. The extended lattice in zeolites provides electrostatic stabilization for carbocations, freeing them to isomerize into products that could not have been easily determined by the earlier rate-determining TS. The occurrence of this electrostatic stabilization leads to a conclusion similar to that reached by Shapovalov and Bell[75] and by Bucko and Hafner[36,76] in studies which also saw relatively flat PESs. Because the metastable intermediate can take on many configurations within the relatively uniform stabilizing potential, the distribution of products will result from the reactivity of this metastable state. This rate-limiting step effectively sets which C−C bond will break but offers ambiguous information on which hydrocarbon fragments will end up as alkanes or alkenes. This isomerization occurs for periods up to about 1 ps in this study, although a few trajectories still yielded the quasistable C−H−C carbocation at 1 ps. During the time immediately following protonation of the C2−C3 bond, the apparent position of the hydrocarbon double bond can shift, and neither ethene or propene appears to be overwhelmingly favored in TS2−3. Sampling of these degrees of dynamic freedom—especially in vibrations orthogonal to the TS mode—determines the resultant isomers when the carbocation eventually deprotonates. Figures 8 and 9 exemplify the dynamics occurring in C5 cracking and suggest the existence of similarly diverse trajectories in other zeolite-catalyzed hydrocarbon reactions.

Shape-selective environments in zeolites deserve considerably more theoretical exploration due to the effect of dynamics. Comparative study of different zeolites catalyzing the same reaction will provide further insight into the complexity of these reactions, and general principles of the role of post-TS dynamics can be brought out. The development of these dynamic principles will further accelerate progress toward the goal of designing zeolite structures that catalyze specific reactions with high rates and selectivity.

ASSOCIATED CONTENT

Ⓢ Supporting Information

A description of the relative rates of ethene and propene formation on the static PES and the complete citation for ref 66. This material is available free of charge via the Internet at http://pubs.acs.org.

AUTHOR INFORMATION

Corresponding Author

mhg@cchem.berkeley.edu; bell@cchem.berkeley.edu

Notes

The authors declare no competing financial interest.

ACKNOWLEDGMENTS

REFERENCES

(1) Kissin, Y. V. *Catal. Rev.* **2001**, *43*, 85.

(2) Haag, W. O.; Dessau, R. M. *Proceedings of the 8th International Congress of Catalysis, Frankfurt-am-Main* **1984**, 305.

(3) Kotrel, S.; Knozinger, H.; Gates, B. C. *Microporous Mesoporous Mater.* **2000**, 35−36, 11.

(4) Corma, A. *Chem. Rev.* **1995**, 95, 559.

(5) Corma, A. *Chem. Rev.* **1997**, 97, 2373.

(6) Keil, F. J. *Top. Curr. Chem.* **2012**, 307, 69.

(7) Williams, B. A.; Ji, W.; Miller, J. T.; Snurr, R. Q.; Kung, H. H. *Appl. Catal. A: Gen.* **2000**, 203, 179.

(8) Jentoft, F. C.; Gates, B. C. *Top. Catal.* **1997**, 4, 1.

(9) Krannila, S.; Rosynek, M. P.; Lunsford, J. H. *J. Catal.* **1992**, 135, 115.

(10) Corma, A.; Orchilles, A. V. *Microporous Mesoporous Mater.* **2000**, 35−36, 21.

(11) De Moor, B. A.; Reyniers, M.-F.; Gobin, O. C.; Lercher, J. A.; Marin, G. B. *J. Phys. Chem. C* **2011**, 115, 1204.

(12) Greensfelder, B. S.; Voge, H. H. *Ind. Eng. Chem. Res.* **1949**, 41, 2573.

(13) Thomas, C. L. *Ind. Eng. Chem. Res.* **1949**, 41, 2564.

(14) Gounder, R.; Iglesia, E. *Acc. Chem. Res.* **2012**, 45, 229.

(15) Gounder, R.; Iglesia, E. *Angew. Chem., Int. Ed.* **2010**, 49, 808.

(16) Babitz, S. M.; Williams, B. A.; Miller, J. T.; Snurr, R. Q.; Haag, W. O.; Kung, H. H. *Appl. Catal. A: Gen.* **1999**, 179, 71.

(17) Wielers, A. F. H.; Vaarkamp, M.; Post, M. F. M. *J. Catal.* **1991**, 127, 51.

(18) Ramachandran, C. E.; Williams, B. A.; van Bokhoven, J. A.; Miller, J. T. *J. Catal.* **2005**, 233, 100.

(19) Kotrel, S.; Rosynek, M. P.; Lunsford, J. H. *J. Phys. Chem. B* **1999**, 103, 818.

(20) Borges, P.; Ramos Pinto, R.; Lemos, M. A. N. D. A.; Lemos, F.; Vedrine, J. C.; Derouane, E. G.; Ramoa Ribeiro, F. *J. Mol. Cat. A: Chem.* **2005**, 229, 127.

(21) Ono, Y.; Kanae, K. *J. Chem. Soc. Faraday Trans.* **1991**, 87, 663.

(22) Swisher, J. A.; Hansen, N.; Maesen, T.; Keil, F. J.; Smit, B.; Bell, A. T. *J. Phys. Chem. C* **2010**, 114, 10229−10239.

(23) Zygmunt, S. A.; Curtiss, L. A.; Zapol, P.; Iton, L. E. *J. Phys. Chem. B* **2000**, 104, 1944.

(24) Zheng, X.; Blowers, P. *J. Phys. Chem. A* **2006**, 110, 2455.

(25) Zheng, X.; Blowers, J. *Mol. Cat. A: Chem.* **2005**, 229, 77.

(26) Rigby, A. M.; Kramer, G. J.; van Santen, R. A. *J. Catal.* **1997**, 170, 1.

(27) Hunter, K. C.; Seitz, C.; East, A. L. L. *J. Phys. Chem. A* **2003**, 107, 159.

(28) Milas, I.; Nascimento, M. A. C. *Chem. Phys. Lett.* **2006**, 418, 368.

(29) Collins, S. J.; O'Malley, P. J. *Chem. Phys. Lett.* **1995**, 246, 555.

(30) Caeiro, G.; Carvalho, R. H.; Wang, X.; Lemos, M. A. N. D. A; Femos, F.; Guisnet, M.; Ramoa Ribeiro, F. *J. Mol. Cat. A: Chem.* **2006**, 255, 131.

(31) Mills, G.; Jónsson, H. *Phys. Rev. Lett.* **1994**, 72, 1124.

(32) Henkelman, G.; Jonsson, H. *J. Chem. Phys.* **2000**, 113, 9978.

(33) Peters, B.; Heyden, A.; Bell, A. T.; Chakraborty, A. *J. Chem. Phys.* **2004**, 120, 7877.

(34) Behn, A.; Zimmerman, P. M.; Bell, A. T.; Head-Gordon, M. *J. Chem. Phys.* **2011**, 135, 224108.

(35) Behn, A.; Zimmerman, P. M.; Bell, A. T.; Head-Gordon, M. *J. Chem. Theor. Comput.* **2011**, 7 (12), 4019.

(36) Bucko, T.; Hafner, J. *J. Phys.: Condens. Matter* **2010**, 22, 384201 (TPS-ish CHA PW91).

(37) Dellago, C.; Bolhuis, P. G. *Adv. Polym. Sci.* **2011**, 1−67. Bolhuis, P. G.; Chandler, D.; Dellago, C.; Geissler, P. L. *Annu. Rev. Phys. Chem.* **2002**, 53, 291.

(38) Bucko, T.; Benco, L.; Hafner, J.; Angyan, J. G. *J. Catal.* **2011**, 279, 220.

(39) Porter, R. N.; Raff, L. M. In *Dynamics of Molecular Collisions, Part B*; Miller, W. H., Ed.; Plenum Press: New York, 1976.

(40) Stewart, J. J. P.; Davis, L. P.; Burggraf, L. W. *J. Comput. Chem.* **1987**, 8, 1117.

(41) Lambrecht, D. S.; Clark, G. N. I.; Head-Gordon, T.; Head-Gordon, M. *J. Phys. Chem. A* **2011**, 115, 5928.

(42) Ramos-Cordoba, E.; Lambrecht, D. S.; Head-Gordon, M. *Faraday Discuss.* **2011**, 150, 345.

(43) Yamada, T.; Aida, M. *J. Phys. Chem. A* **2010**, 114, 6273.

(44) Ess, D. H.; Wheeler, S. E.; Iafe, R. G.; Xu., L.; Celebi-Olcum, N.; Houk, K. N. *Angew. Chem., Int. Ed.* **2008**, 47, 7592.

(45) Zimmerman, P. M.; Zhang, Z.; Musgrave, C. B. *J. Phys. Chem. Lett.* **2011**, 2, 276.

(46) Vayner, G.; Addepalli, S. V.; Song, K.; Hase, W. L. *J. Chem. Phys.* **2006**, 125, 014317.

(47) Lourderaj, U.; Park, K.; Hase, W. L. *Int. Rev. Phys. Chem.* **2008**, 27, 361. Sun, L.; Song, K.; Hase, W. L. *Science* **2002**, 296, 875.

(48) Lopez, J. G.; Vayner, G.; Lourderaj, U.; Addepalli, S. V.; Kato, S.; de Jong, W. A.; Windus, T. L.; Hase, W. L. *J. Am. Chem. Soc.* **2007**, 129, 9976−9985.

(49) Haag, W. O.; Lago, R. M. *Nature* **1984**, 309, 589.

(50) Smit, B.; Maesen, T. L. M. *Nature* **2008**, 451, 671.

(51) Maesen, T. L. M.; Beerdsen, E.; Calero, S.; Dubbeldam, D.; Smit, B. *J. Catal.* **2006**, 237, 278.

(52) van Santen, R. A.; Offermans, W. K.; Malek, K.; Pidko, E. A. *Mol. Simul.* **2007**, 33, 327.

(53) Hansen, N.; Krishna, R.; van Baten, J. M.; Bell, A. T.; Keil, F. J. *J. Phys. Chem. C* **2009**, 113, 235.

(54) Heyden, A.; Hansen, N.; Bell, A. T.; Keil, F. J. *J. Phys. Chem. B* **2006**, 110, 17096.

(55) Broadbelt, L. J.; Snurr, R. Q. *Appl. Catal., A* **2000**, 200, 23.

(56) Zimmerman, P. M.; Head-Gordon, M.; Bell, A. T. *J. Chem. Theory Comput.* **2011**, 7, 1695−1703.

(57) Abouelnasr, M. K. F.; Smit, B. *Phys. Chem. Chem. Phys.* **2012**, 14, 11600.

(58) Gomes, J.; Zimmerman, P. M.; Head-Gordon, M.; Bell, A. T. *J. Phys. Chem. C* **2012**, 116, 15406.

(59) Olson, D. H.; Kokotailo, G. T.; Lawton, S. L.; Meier, W. M. *J. Phys. Chem.* **1981**, 85, 2238−2243.

(60) Olson, D. H.; Khosrovani, N.; Peters, A. W.; Toby, B. H. *J. Phys. Chem. B* **2000**, 104, 4844−4848.

(61) Mentzen, B. F.; Sacerdote-Peronnet, M. *Mater. Res. Bull.* **1994**, 29, 1341−1348.

(62) Grimme, S. *J. Comput. Chem.* **2006**, 27, 1787−99.

(63) (a) Foloppe, N.; MacKerell, A. D. *J. Comput. Chem.* **2000**, 21, 86−104. (b) Yin, D.; MacKerell, A. D. *J. Comput. Chem.* **1998**, 19, 334−348. (c) Vanommeslaeghe, K.; Hatcher, E.; Acharya, C.; Kundu, S.; Zhong, S.; Shim, J.; Darian, E.; Guvench, O.; Lopes, P.; Vorobyov, I.; MacKerell, A. D. *J. Comput. Chem.* **2010**, 31, 671−690.

(64) (a) Chai, J.-D.; Head-Gordon, M. *Phys. Chem. Chem. Phys.* **2008**, 10, 6615−6620. (b) Chai, J.-D.; Head-Gordon, M. *J. Chem. Phys.* **2008**, 128, 084106.

(65) Gonzalez, C.; Schlegel, H. B. *J. Chem. Phys.* **1989**, 90, 2154.

(66) Shao, Y.; et al. *Phys. Chem. Chem. Phys.* **2006**, 8, 3172−3191.

(67) Sun, L; Hase, W. L. *J. Chem. Phys.* **2010**, 133, 044313/1−9.

(68) Prigogine, I.; Rice, S. A.; Peslherbe, G. H.; Wang, H.; Hase, W. L. *Adv. Chem. Phys.* **1999**, 105, 171.

(69) Sun, L.; Park, K.; Song, K.; Setser, D. W.; Hase, W. L. *J. Chem. Phys.* **2006**, 124, 064313.

(70) Hunter, K. C.; East, A. L. L. *J. Phys. Chem. A* **2002**, 106, 1346.

(71) Narbeshuber, T. F.; Vinek, H.; Lercher, J. A. *J. Catal.* **1995**, 157, 388.

(72) Narbeshuber, T. F.; Brait, A.; Seshan, K.; Lercher, J. A. *J. Catal.* **1997**, 172, 127.

(73) Denayer, J. F.; Souverijns, W.; Jacobs, P. A.; Martens, J. A.; Baron, G. V. *J. Phys. Chem. B* **1998**, 102, 4588−4597.

(74) Haas, K.; Chu, J.-W. *J. Chem. Phys.* **2009**, 131, 144105.

(75) Shapovalov, V.; Bell, A. T. *J. Phys. Chem. C* **2010**, 114 (41), 17753−17760.

(76) Bucko, T.; Benco, L.; Dubay, O.; Dellago, C.; Hafner, J. *J. Chem. Phys.* **2009**, 131, 214508.